Draft version May 24, 2012
Preprint typeset using LaTeX style emulateapj v. 5/2/11

arXiv:1111.4219v2 [astro-ph.HE] 23 May 2012

ON HYDROMAGNETIC STRESSES IN ACCRETION DISK BOUNDARY LAYERS

Martin E. Pessah[1] and Chi-kwan Chan[2]
[1]Niels Bohr International Academy, Niels Bohr Institute, Blegdamsvej 17, 2100 Copenhagen Ø, Denmark; mpessah@nbi.dk
[2]NORDITA, Roslagstullsbacken 23, 106 91 Stockholm, Sweden; ckch@nordita.org
Draft version May 24, 2012

ABSTRACT

Detailed calculations of the physical structure of accretion disk boundary layers, and thus their inferred observational properties, rely on the assumption that angular momentum transport is opposite to the radial angular frequency gradient of the disk. The standard model for turbulent shear viscosity satisfies this assumption by construction. However, this behavior is not supported by numerical simulations of turbulent magnetohydrodynamic (MHD) accretion disks, which show that angular momentum transport driven by the magnetorotational instability (MRI) is inefficient in disk regions where, as expected in boundary layers, the angular frequency increases with radius. In order to shed light into physically viable mechanisms for angular momentum transport in this inner disk region, we examine the generation of hydromagnetic stresses and energy density in differentially rotating backgrounds with angular frequencies that increase outward in the shearing-sheet framework. We isolate the modes that are unrelated to the standard MRI and provide analytic solutions for the long-term evolution of the resulting shearing MHD waves. We show that, although the energy density of these waves can be amplified significantly, their associated stresses oscillate around zero, rendering them an inefficient mechanism to transport significant angular momentum (inward). These findings are consistent with the results obtained in numerical simulations of MHD accretion disk boundary layers and challenge the standard assumption of efficient angular momentum transport in the inner disk regions. This suggests that the detailed structure of turbulent MHD accretion disk boundary layers could differ appreciably from those derived within the standard framework of turbulent shear viscosity.

Subject headings: accretion, accretion disks — instabilities — magnetohydrodynamics (MHD) — turbulence

1. INTRODUCTION

Basic arguments suggest that the angular frequency $\Omega(r)$ of an accretion disk surrounding a weakly magnetized star must attain a maximum value, $\Omega_{\rm max} \equiv \Omega(r_{\rm b})$, and decrease inward (or at least remain constant; see Medvedev 2004) to match the angular frequency of the star at the stellar radius $\Omega_\star(r_\star)$; see, e.g., Frank et al. (2002); Hartmann (2009); Armitage (2010). The inner disk region, where $r < r_{\rm b}$ and $d\Omega/dr \geq 0$, is referred to as the accretion disk *boundary layer*. Standard accretion disk theory (Shakura & Sunyaev 1973) predicts that half of the energy released in the accretion process takes place in this region, estimated to be a fraction of the stellar radius. The spectrum of the radiated energy depends on the detailed properties of this layer (Narayan & Popham 1993; Popham & Narayan 1995; Popham et al. 1996; Popham & Sunyaev 2001); thus understanding the various processes that determine its properties (see, e.g., Piro & Bildsten 2004; Balsara et al. 2009; Inogamov & Sunyaev 2010) is of fundamental importance.

Most detailed calculations for determining the structure of the boundary layer rely on effective models for turbulent angular momentum transport. These models are usually built as a turbulent version of the Newtonian viscous stress between fluid layers in a differentially rotating laminar flow (Landau & Lifshitz 1959), and thus assume a linear relationship between the stress and the angular frequency gradient (Lynden-Bell & Pringle 1974). This assumption, however, seems at odds with the properties of magnetohydrodynamic (MHD) turbulence revealed by numerical simulations of accretion disks (Abramowicz et al. 1996; Armitage 2002; Steinacker & Papaloizou 2002; Pessah et al. 2008) which show that angular momentum transport is inefficient in regions of the disk where $d\Omega/dr > 0$, which are stable to the standard magnetorotational instability (MRI; see Balbus & Hawley 1991, 1998).

Motivated by the need of a deeper understanding of the behavior of an MHD fluid in a differentially rotating background that deviates from a Keplerian profile, we study the dynamics of MHD waves in configurations that are stable to the standard MRI. Employing the shearing-sheet framework, we show that transient amplification of shearing MHD waves can generate magnetic energy without leading to a substantial generation of hydromagnetic stresses. We discuss the implications of these findings.

2. ASSUMPTIONS AND LOCAL MODEL FOR MHD DISK

We focus our attention on a subsonic, weakly magnetized fluid for which the ram pressure and magnetic pressure remain small compared to their thermal counterpart. As a first approximation, we thus consider a differentially rotating fluid with angular frequency $\boldsymbol{\Omega} = \Omega(r)\check{\boldsymbol{z}}$ and constant background density ρ_0. This is a reasonable assumption in light of the results presented by Armitage (2002) and Steinacker & Papaloizou (2002), who carried out numerical simulations of boundary layers of unstratified accretion disks and found that the density fluctuations throughout the simulations are in general quite small.

We work in the framework of the shearing-sheet approximation (Hill 1878; Goldreich & Tremaine 1978; Narayan et al. 1987; Hawley et al. 1995), where the equations describing an incompressible MHD fluid in a corotating frame are given by

$$\partial_t \boldsymbol{v} + (\boldsymbol{v}\cdot\nabla)\boldsymbol{v} = -2\Omega_0\check{\boldsymbol{z}}\times\boldsymbol{v} + 2q\Omega_0^2 x\check{\boldsymbol{x}} - \frac{\nabla P}{\rho_0} + \frac{(\boldsymbol{B}\cdot\nabla)\boldsymbol{B}}{4\pi\rho_0} + \nu\nabla^2\boldsymbol{v}\,, \tag{1}$$

$$\partial_t \boldsymbol{B} + (\boldsymbol{v}\cdot\nabla)\boldsymbol{B} = (\boldsymbol{B}\cdot\nabla)\boldsymbol{v} + \eta\nabla^2\boldsymbol{B}\,. \tag{2}$$

Here, $\boldsymbol{v}(\boldsymbol{x},t)$ and $\boldsymbol{B}(\boldsymbol{x},t)$, with $\nabla\cdot\boldsymbol{v}=\nabla\cdot\boldsymbol{B}=0$, stand for the velocity and magnetic fields; ν and η denote the kinematic viscosity and resistivity; and $\Omega_0\equiv\Omega(r_0)$ is the corotating angular frequency at a fiducial radius r_0. The first and second terms on the right hand side of equation (1) correspond to the Coriolis and tidal forces, respectively. The local pressure P can be found by the divergence-less condition of the velocity field. Recalling that the local density ρ_0 is assumed to be constant, and in order to simplify notation, hereafter we redefine the symbols denoting the pressure and magnetic field in such a way that and $P/\rho_0\to P$ and $\boldsymbol{B}/(4\pi\rho_0)^{1/2}\to\boldsymbol{B}$.

We decompose the flow into mean and fluctuations as

$$\boldsymbol{v}(\boldsymbol{x},t)\equiv\boldsymbol{U}_1(x)+\boldsymbol{u}(\boldsymbol{x},t), \tag{3}$$
$$\boldsymbol{B}(\boldsymbol{x},t)\equiv\boldsymbol{B}_0(t)+\boldsymbol{b}(\boldsymbol{x},t). \tag{4}$$

The leading order background velocity is $\boldsymbol{U}_1(x)\equiv-q\,\Omega_0 x\check{\boldsymbol{y}}$, where the shear parameter q is given by

$$q\equiv-\left.\frac{d\ln\Omega}{d\ln r}\right|_{r_0}. \tag{5}$$

The homogeneous background magnetic field is in general a function of time and it evolves according to the induction equation (2), i.e., $\partial_t\boldsymbol{B}_0=-q\,\Omega_0 B_{0x}\check{\boldsymbol{y}}$.

The substitution of equations (3) and (4) into (1) and (2) leads to a non-linear system for the dynamical evolution of the perturbations $\boldsymbol{u}(\boldsymbol{x},t)$ and $\boldsymbol{b}(\boldsymbol{x},t)$. However, as pointed out in Goodman & Xu (1994), all the non-linear terms in the resulting equations vanish identically if we consider the evolution of a single Fourier mode[1]. In this case we obtain

$$\mathcal{D}_t\boldsymbol{u}-q\,\Omega_0 u_x\check{\boldsymbol{y}}=\boldsymbol{B}_0\cdot\nabla\boldsymbol{b}+\nu\nabla^2\boldsymbol{u}-2\Omega_0\check{\boldsymbol{z}}\times\boldsymbol{u}-\nabla P, \tag{6}$$
$$\mathcal{D}_t\boldsymbol{b}+q\,\Omega_0 b_x\check{\boldsymbol{y}}=\boldsymbol{B}_0\cdot\nabla\boldsymbol{u}+\eta\nabla^2\boldsymbol{b}. \tag{7}$$

The "semi-Lagrangian" time derivative $\mathcal{D}_t\equiv\partial_t+\boldsymbol{U}_1\cdot\nabla$ accounts for advection by the shearing background. The shearing component in the Coriolis term cancels out the tidal force. We remark that equations (6) and (7) are *not* just linearized equations, they remain valid even if the amplitude of the perturbations is not small compared to the background values, and they are exact as long as a single Fourier mode is considered. Under these conditions, it is sensible to study the evolution of $\boldsymbol{u}(\boldsymbol{x},t)$ and $\boldsymbol{b}(\boldsymbol{x},t)$ for a long time.

In order to solve equations (6) and (7), it is convenient to work in Fourier space. The x-dependence of the "semi-Lagrangian" time derivative can be removed by employing a shearing coordinate system $(x',y',z',t')\equiv(x,y+q\,\Omega_0 xt,z,t)$ in which $\mathcal{D}_t=\partial_{t'}$ (Goldreich & Lynden-Bell 1965). A single mode with a fixed "shearing" wavenumber $\boldsymbol{k}'$ is thus given by

$$\boldsymbol{u}(\boldsymbol{x},t)=2\mathrm{Re}\left[\hat{\boldsymbol{u}}_{\boldsymbol{k}'}(t)\exp(i\boldsymbol{k}'\cdot\boldsymbol{x}')\right], \tag{8}$$
$$\boldsymbol{b}(\boldsymbol{x},t)=2\mathrm{Re}\left[\hat{\boldsymbol{b}}_{\boldsymbol{k}'}(t)\exp(i\boldsymbol{k}'\cdot\boldsymbol{x}')\right], \tag{9}$$

where $\boldsymbol{k}'\cdot\boldsymbol{x}'=\boldsymbol{k}(t)\cdot\boldsymbol{x}=(k'_x+q\,\Omega_0 tk'_y)x+k'_y y+k'_z z$.

Substituting the ansatz (8) and (9) into equations (6) and (7) leads a set of equations for the Fourier amplitudes

$$d_t\hat{\boldsymbol{u}}-q\,\Omega_0\hat{u}_x\check{\boldsymbol{y}}=i\omega_{\rm A}\hat{\boldsymbol{b}}-\nu k^2\hat{\boldsymbol{u}}-2\Omega_0\check{\boldsymbol{z}}\times\hat{\boldsymbol{u}}-i\boldsymbol{k}\hat{P}, \tag{10}$$
$$d_t\hat{\boldsymbol{b}}+q\,\Omega_0\hat{b}_x\check{\boldsymbol{y}}=i\omega_{\rm A}\hat{\boldsymbol{u}}-\eta k^2\hat{\boldsymbol{b}}. \tag{11}$$

Here, we have replaced $\partial_{t'}$ by d_t and omitted the subscripts $\boldsymbol{k}'$ in the Fourier coefficients in order to simplify the notation.

[1] Formally speaking we consider two modes, with wavenumbers $\boldsymbol{k}$ and $-\boldsymbol{k}$. However, because the functions under consideration are real, the Fourier coefficients satisfy $\hat{f}_{-\boldsymbol{k}}=\hat{f}^*_{\boldsymbol{k}}$.

We have also introduced the (time-independent) Alfvén frequency $\omega_{\rm A}\equiv\boldsymbol{B}_0(t)\cdot\boldsymbol{k}(t)$ (see also Balbus & Hawley 1992a).

The pressure term can be eliminated from equation (10) using the solenoidal character of the velocity field, which implies $d_t i\boldsymbol{k}=i\boldsymbol{k}d_t+iq\,\Omega_0 k_y\check{\boldsymbol{x}}$. This leads to

$$\hat{P}=-\frac{2i\Omega_0}{k^2}\Big[(q-1)k_y\hat{u}_x+k_x\hat{u}_y\Big], \tag{12}$$

which is independent of $\hat{u}_z$. Because we are interested in the transport of angular momentum along the radial direction, this decoupling allows us to solve separately for the x- and y-components.

3. DYNAMICAL EVOLUTION OF MRI-STABLE MODES

The dynamical evolution of the modes with $\boldsymbol{k}\equiv k_z\check{\boldsymbol{z}}$ is quite simple; they grow exponentially if $k_z^2\omega_{\rm A}^2\le 2q\Omega_0^2$ (Balbus & Hawley 1992b; Pessah et al. 2006). Thus, a Keplerian disk (with $q=3/2$) can exhibit exponential growth but a shear profile with $q<0$ only supports stable oscillations. In order to isolate the interesting dynamics that could arise from modes that are not associated with the MRI, we thus focus on modes with $k_z=0$. Taking the curl of the momentum equation, it is easy to verify that the Coriolis term does not play a role in the equation for the vorticity, and hence it has no effect on the dynamics of the system (Lithwick 2007). This shows explicitly that the standard MRI is absent in our analysis.

We choose the origin of time so that $k_x(t)$ is initially zero. In other words, we use $k_x(t)$ to define our time coordinate,

$$\tau\equiv k_x(t)/k_y\equiv q\,\Omega_0 t\,, \tag{13}$$

so the divergence-less conditions become

$$\tau\,\hat{u}_x+\hat{u}_y=\tau\,\hat{b}_x+\hat{b}_y=0. \tag{14}$$

Assuming $\nu,\eta\ll\omega_{\rm A}/k^2$, we can work in the ideal limit and neglect viscosity and resistivity. The x-components of the MHD equations then become

$$d_\tau\begin{pmatrix}\hat{u}_x\\ \hat{b}_x\end{pmatrix}=\begin{pmatrix}-\Gamma & i\omega\\ i\omega & 0\end{pmatrix}\begin{pmatrix}\hat{u}_x\\ \hat{b}_x\end{pmatrix}, \tag{15}$$

where all the temporal dependence is contained in the factor

$$\Gamma(\tau)\equiv 2\tau/(\tau^2+1), \tag{16}$$

and

$$\omega\equiv\omega_{\rm A}/q\,\Omega_0 \tag{17}$$

is the dimensionless Alfvén frequency. The linear system (15) can be recast into one equation as

$$d_\tau^2\hat{b}_x+\Gamma(\tau)\,d_\tau\hat{b}_x+\omega^2\hat{b}_x=0, \tag{18}$$

where the dependence on the parameters q, Ω_0, and $\omega_{\rm A}$ is *only* through the combination $(\omega_{\rm A}/q\,\Omega_0)^2$. This second order differential equation for $\hat{b}_x$ is identical to equation (2.20) in Balbus & Hawley (1992a) when $k_z=0$. In this case, the perturbations in the z-coordinate decouple from the perturbations in the perpendicular direction, see also their equation (2.19).

Unfortunately, equation (18) does not have an analytical solution. However, if we consider the limit $\tau^2\gg 1$, it reduces to

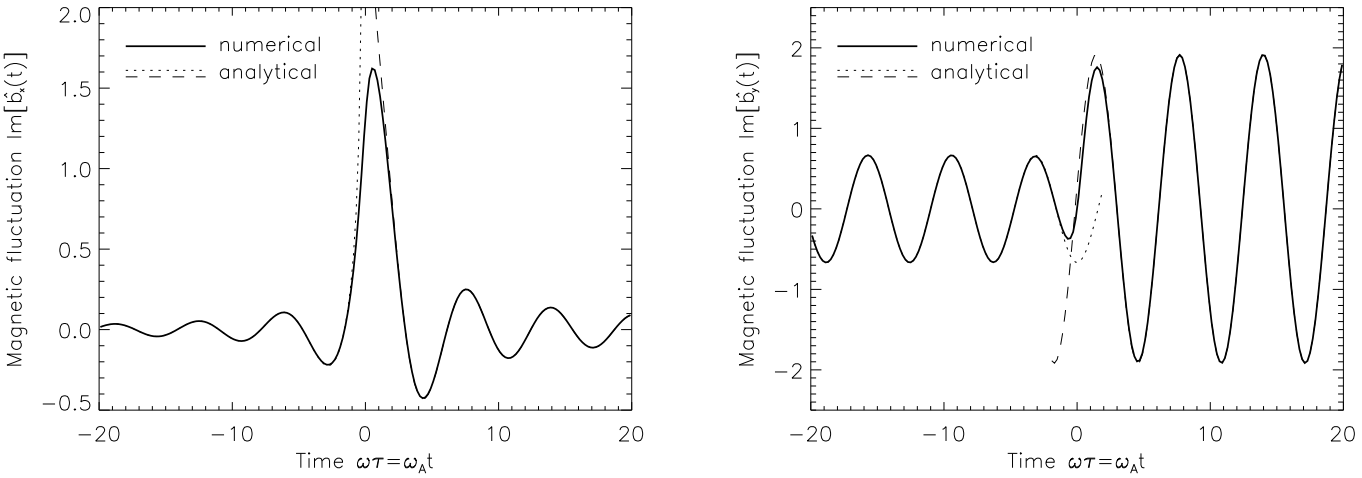


Figure 1. The Fourier amplitudes for the magnetic field components $\hat{b}_x$ (left) and $\hat{b}_y$ (right). The thick solid lines are the numerical solutions obtained by solving equation (18) with $q = -3/2$ and $\omega_A = \Omega_0$ and using the divergence-less conditions (14). The asymptotic solutions for early and late times are both given by the analytical approximation (20) and (22) but with different integration constants. The dotted lines correspond to $C_- = 1$ and $S_- = 0$, which are used to specify the initial conditions at $\omega\tau = -20$. The dashed lines correspond to $C_+ = 0.285$ and $S_+ = -1.896$, which are obtained by matching the analytic and numerical results at late times, e.g., $\omega\tau = 20$. Note that, for the sake of clarity, we truncate the analytical solutions in the right panel at $\omega\tau = 2$ and -2.

a spherical Bessel equation, which posseses as solutions

$$\begin{aligned}\hat{u}_x &= S\, j_1(\omega\tau) + C y_1(\omega\tau),\\ &= -\frac{C + S\omega\tau}{\omega^2\tau^2}\cos(\omega\tau) + \frac{S - C\omega\tau}{\omega^2\tau^2}\sin(\omega\tau), \qquad (19)\\ \hat{b}_x &= -iS\, j_0(\omega\tau) - iC y_0(\omega\tau)\\ &= \frac{iC}{\omega\tau}\cos(\omega\tau) - \frac{iS}{\omega\tau}\sin(\omega\tau), \qquad (20)\end{aligned}$$

where $j_n(x)$ and $y_n(x)$, with $n = 0, 1$, are spherical Bessel functions of the first and second kind, respectively; and S and C are complex constants determined by the initial conditions. Using the divergence-less conditions in equation (14), the y-components are simply

$$\begin{aligned}\hat{u}_y &= -\tau\,[S\, j_1(\omega\tau) + C y_1(\omega\tau)]\\ &= \frac{C + S\omega\tau}{\omega^2\tau}\cos(\omega\tau) - \frac{S - C\omega\tau}{\omega^2\tau}\sin(\omega\tau), \qquad (21)\\ \hat{b}_y &= i\tau\,[S\, j_0(\omega\tau) + C y_0(\omega\tau)]\\ &= -\frac{iC}{\omega}\cos(\omega\tau) + \frac{iS}{\omega}\sin(\omega\tau). \qquad (22)\end{aligned}$$

Because the pressure in equation (12) is independent of $\hat{u}_z$, the exact solutions (for all time) are Alfvén waves,

$$\begin{aligned}\hat{u}_z &= C'\cos(\omega\tau) + S'\sin(\omega\tau), \qquad (23)\\ \hat{b}_z &= iC'\sin(\omega\tau) - iS'\cos(\omega\tau), \qquad (24)\end{aligned}$$

where C' and S' are some other complex constants. We note that, although the direction of the dimensionless time τ depends on the sign of the shear parameter q, the combination $\omega\tau \equiv \omega_A t$ is insensitive to it. Hence, given the same initial conditions, $\hat{u}_x$ and $\hat{b}_x$ are symmetric, while $\hat{u}_y$ and $\hat{b}_y$ are antisymmetric, in the shear parameter q.

We demonstrate the accuracy of these analytical approximations in Figure 1, which shows both the numerical and analytical solutions for Im[$\hat{b}_x$] and Im[$\hat{b}_y$] with $q = -3/2$ and $\omega_A = \Omega_0$ as an example. The initial conditions are set at $\omega\tau = \omega_A t = -20$ by choosing $C_- = 1$ and $S_- = 0$. The numerical solutions, shown with thick solid lines, result from integrating equation (18) with the definition (16) and using the divergence-less conditions (14). The dotted lines in the two panels are obtained by setting $C = C_-$ and $S = S_-$ in the analytical approximations (20) and (22). These solutions are indistinguishable for $\tau \lesssim -1$. As expected, the approximations break down for $\tau \simeq 0$. This is precisely where the numerical solutions change their amplitudes significantly. The analytical expressions (20) and (22) are again in excellent agreement with the numerical solutions for $\tau \gtrsim 1$, provided that their amplitudes are given by $C = C_+ = 0.285$ and $S = S_+ = -1.896$. These constants are found by requiring that both the numerical and analytical solutions match for $\omega\tau = \omega_A t \gg 1$ (in practice we set $\omega\tau = 20$).

Even though our analytical approach cannot predict the change in amplitude close to $\tau \approx 0$, the solutions that we obtain are a very good approximation to the numerical results as long as $\tau^2 > 1$. We could in principle obtain the coefficients C_+ and S_+ by an asymptotic matching technique similar to the one employed in Heinemann & Papaloizou (2009). However, the analytical solution near $\tau \simeq 0$ contains special functions that are too complicated to be useful. More importantly, as we show below, the most interesting features of the solutions are independent of the precise values of these constants.

4. LATE TIME STRESS AND ENERGY

Given the solutions (19) – (24) for the Fourier amplitudes, we obtain the (mean) total stress $T_{xy} \equiv \langle u_x u_y - b_x b_y\rangle$ and (mean) energy density $E \equiv \langle u^2 + b^2\rangle/2$ of the fluctuating fields[2], where the brackets stand for the spatial average, see, e.g., Pessah et al. (2006). Because these solutions are only valid for early/late times, we can approximate the total stress and energy density up to first order in $1/\omega\tau$ as

$$T_{xy} \approx -\frac{2}{\omega^2\tau}\Big[(|S|^2 - |C|^2)\cos(2\omega\tau) + (S^*C + SC^*)\sin(2\omega\tau)\Big], \qquad (25)$$

$$E \approx -\frac{1}{\omega^3\tau}\Big[(|S|^2 - |C|^2)\sin(2\omega\tau) - (S^*C + SC^*)\cos(2\omega\tau)\Big] + \frac{1}{\omega^2}\left(|S|^2 - |C|^2\right) + |S'|^2 + |C'|^2\,, \qquad (26)$$

where the asterisk denotes complex conjugation. Using these expressions, it is easy to see that the energy balance equation $d_t E = q\Omega_0 T_{xy}$ is also satisfied up to order $1/\omega\tau$.

[2] We do not include the stress and energy generated by the time-dependent mean field $\boldsymbol{B}_0(t)$ here. This contribution depends on the initial magnetic field.

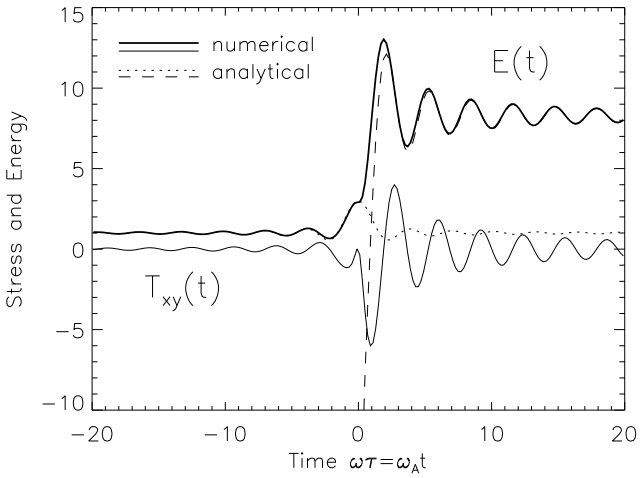


Figure 2. The thick and thin solid lines correspond, respectively, to the total energy $E(t)$ and total stress $T_{xy}(t)$, calculated using the Fourier amplitudes $\hat{u}_x$, $\hat{u}_y$, $\hat{b}_x$, and $\hat{b}_y$ obtained numerically. The dotted and dashed lines show the analytical approximation for the energy, equation (26), using the two sets of constants described in the caption of Figure 1. The x-components of the velocity and magnetic fields are symmetric in q but the y-components are anti-symmetric. Therefore, changing the sign of the shear parameter q changes the sign of the stress T_{xy} but not of the energy E.

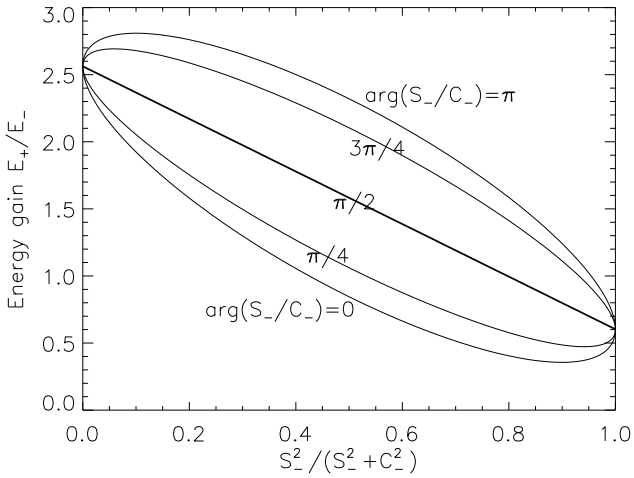


Figure 3. The solid curves show the dependence of the energy gain, E_+/E_-, on the initial conditions for $\omega = \omega_A/q\Omega_0 = 1$. The horizontal axis provides a measure of the relative amplitude of C_- and S_-; while the different lines show the results for various phase differences. For strong shear $1/\omega^2 > 1$, the dependence of the phase is weaker and all the different curves collapse onto the straight thick line, which corresponds to $\arg(S_-/C_-) = \pi/2$, while this one gets steeper, thus providing a larger energy gain, see also Figure 4.

In Figure 2, we illustrate the numerical solutions for the stress $T_{xy}(t)$ and energy $E(t)$, given by the thin and thick solid lines, together with the analytical approximation for the energy. The latter has been obtained by substituting the two pairs of constants, $C_- = 1$ and $S_- = 0$, and $C_+ = 0.285$ and $S_+ = -1.896$, into equation (26). It is thus clear that the late-time stress oscillates around zero with decreasing amplitude, while the energy density asymptotes to a non-vanishing, time-independent value. The expression for the energy density at early/late times in terms of the constants $S_\pm$ and $C_\pm$ is given by[3]

$$E_\pm \equiv \lim_{t\to\pm\infty} E(t) = \frac{|S_\pm|^2 + |C_\pm|^2}{\omega^2}\,. \tag{27}$$

Therefore, the energy gain via swing amplification, E_+/E_-, is in general a function of the ratio $\omega = \omega_A/q\Omega_0$ and the initial conditions. However, it is possible to obtain conclusions that are independent of the latter.

The dependence of the energy gain on the initial conditions for $\omega^2 = 1$ is shown in Figure 3. The horizontal axis describes how the initial energy is distributed between the j_n modes and the y_n modes; while the different lines show the phase difference in the corresponding initial amplitudes. When $\arg(S_-/C_-) = \pi/2$ or $3\pi/2$, the j_n and y_n modes are completely out of phase and evolve independently. This results in an energy gain which is linear in the initial amplitudes (thick solid line). We have found that the dependence of the energy gain on the phase difference between the constants determining the initial conditions is weaker if ω decreases below unity. In this case, all the different curves converge to the thick line corresponding to $\arg(S_-/C_-) = \pi/2$. At the same time, as ω decreases below unity, this line gets steeper, providing thus a larger energy gain. This justifies referring to the y_n and j_n as the "growing" and "decaying" modes, respectively.

We illustrate the dependence of the energy gain on the shear parameter in Figure 4 (because the results depend only on ω^2, we only show the positive domain in the horizontal axis). In the limit of weak shear, there are only pure Alfvén waves and there is no net energy gain. The dashed line shows that the energy gain tends to the value $E_+/E_- = 10/\omega^2$ as $1/\omega \gg 1$, which provides a good description of the numerical results for strong shear. The asymptotic behavior is insensitive to the initial conditions as long as the growing mode is excited, i.e. $C_- \neq 0$.

5. DISCUSSION

5.1. *Summary and Connection to Previous Work*

We have employed the shearing-sheet framework to study the dynamical evolution of MHD waves in weakly magnetized differentially rotating backgrounds which are stable to the MRI. While the fact that these waves can be transiently amplified is widely appreciated, our motivation to study them, as well as the results that we obtained, concern dynamical aspects that have not received as much attention. This is whether these shearing MHD waves can play a significant role in the transport of angular momentum in regions of the disk where the MRI is inefficient, such as the accretion disk boundary layer.

The equations that we have solved are similar to those presented in Balbus & Hawley (1992a), who provided numerical solutions showing that transient amplification of MHD waves is a general outcome for the modes with wavevectors that are not exactly aligned with the rotation z-axis[4]. Analytical insight on the non-linear dynamics of these waves has been usually hindered by the fact that the governing equations cannot be simplified beyond a set of coupled differential equations (see, e.g., Fan & Lou 1997; Kim & Ostriker 2000; Brandenburg & Dintrans 2006, and also Johnson 2007, where higher order WKB solutions for the linear evolution of the shearing waves are provided). In this paper, by isolating the modes that are unrelated to the standard MRI, i.e., by setting $k_z = 0$, we have been able to provide analytical solutions that are valid for all times, except close to the instant where the waves evolve from leading to trailing, i.e., when $k_x(t) = 0$. These solutions are exact when only one Fourier mode is considered (Goodman & Xu 1994).

[3] Here, we assume $S' = C' = 0$, and thus avoid the uninteresting contributions due to any stable Alfvén wave initially present, see equations (23)–(24).

[4] For an analysis of non-axisymmetric spiral waves when only a strong, vertical background magnetic field is considered see Tagger et al. (1992).

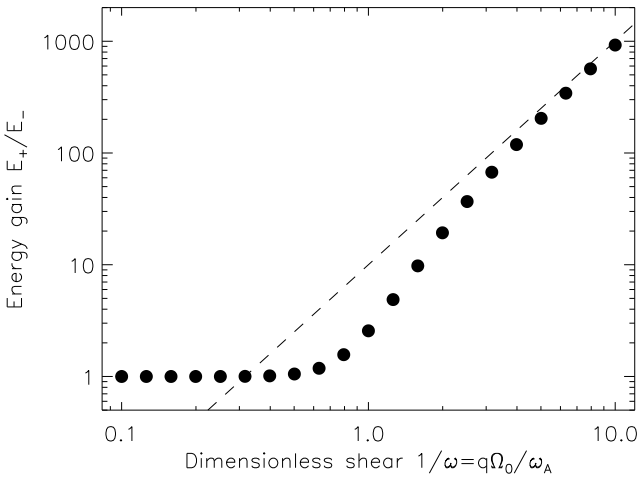


Figure 4. The filled circles represent the value of the energy gain E_+/E_- for different values of the shear, parameterized via $q\Omega_0/\omega_A = 1/\omega$, obtained via numerical integration using the initial conditions $C_- = 1$ and $S_- = 0$, i.e., only the growing mode is excited. In the limit of weak shear, there are only pure Alfvén waves and thus there is no net energy gain. The dashed line shows the function $10/\omega^2 \equiv 10(q\Omega_0/\omega_A)^2$, which is in good agreement with the numerical results for strong shear. This asymptotic behavior is independent of the initial conditions as long as $C_- \neq 0$.

Despite the fact that we do not predict analytically the amplification factor for these waves, the characteristics of the solutions that we found allowed us to draw important conclusions. We showed that the amplification factor is *only* a function of the (time-independent) dimensionless ratio $(q\Omega_0/\omega_A)^2$, with

$$\frac{E_+}{E_-} \approx 10\left(\frac{q\Omega_0}{\omega_A}\right)^2 \quad \text{for} \quad q\Omega_0 \gg \omega_A\,, \tag{28}$$

see equation (27) and Figure 4, and it is thus insensitive to the sign of the shear parameter q.

An important result of this study is that while the energy of these MHD waves can be significantly amplified, their net associated stresses oscillate around zero, see equation (25) and Figure 2. This suggests that these shearing MHD waves are unlikely to play an important role in the transport of angular momentum in the accretion disk boundary layer region. These findings are consistent with the results of global MHD simulations of accretion disks with a rigid inner boundary carried out in Armitage (2002) and Steinacker & Papaloizou (2002). These simulations show that the inner disk regions, where $d\Omega/dr \geq 0$, can develop strong toroidal magnetic fields, with associated magnetic energies that can easily reach a few tenths of the thermal energy, without leading to efficient angular momentum transport.

5.2. *Implications*

The importance of understanding the relationship between the stress and the radial gradient in angular frequency resides in that this dependence plays a key role when modeling the inner structure of an accretion disk surrounding a weekly magnetized star (see, e.g., Popham & Narayan 1995; Popham et al. 1996).

In the steady state, the constant inward flux of angular momentum at any given radius r_0 is given by $\dot{J} = \dot{M}l - 2\pi r_0^2 H T_{r\phi}$, where $\dot{M}$ stands for the accretion rate, l is the specific angular momentum, H is the disk height, and $T_{r\phi}$ (denoted by T_{xy} in our analysis) is the component of the stress responsible for the flux of azimuthal momentum across the radial direction. Thus, the angular momentum flux has two contributions: $\dot{J}_{\rm matter} = \dot{M}l$, which accounts for the flux of angular momentum due to mass accretion, and $\dot{J}_{\rm stress} = -2\pi r_0^2 H T_{r\phi}$, which accounts for the flux of angular momentum due to the stress acting on the fluid elements constituting the disk. Under the reasonable assumption that the disk must be Keplerian well beyond the boundary layer, i.e., for $r \gg r_{\rm b}$, and that the stress should vanish in the absence of shear, we must have $\dot{J} \equiv \dot{M}l(r_{\rm b}) > 0$, i.e., a slowly rotating star accretes mass *and* angular momentum.

In order for this picture to be self-consistent, the stress must satisfy $T_{r\phi}(r_\star \leq r \leq r_{\rm b}) \leq 0$. In the standard accretion disk model this requirement is satisfied by assuming that the stress is linearly proportional to the local shear $T_{r\phi} \sim -d\Omega/dr$. With this model for the stress, and some supplementary assumptions, it is possible to solve for the radial dependence of $\Omega(r)$ and determine the structure of the disk (see, e.g., Popham & Narayan 1991). However, this assumption, broadly adopted in the framework of enhanced turbulent disk viscosity, does not seem to be supported by the modern paradigm, in which angular momentum transport is due to MHD turbulence driven by the MRI. Indeed, both local numerical simulations of shearing-boxes with non-Keplerian shear profiles (Pessah et al. 2008; Snellman et al. 2009) and global disk simulations with a rigid inner boundary (Armitage 2002; Steinacker & Papaloizou 2002) suggest that angular momentum transport is inefficient if $d\Omega/dr > 0$. This suggests that the detailed structure of accretion disk boundary layers resulting from the interaction of an MHD disk with a weakly magnetized star could differ appreciably from those derived within the standard turbulent shear viscosity, where the direction of angular momentum transport is always opposite to the angular frequency gradient.

5.3. *Final Remarks*

It is worth mentioning explicitly that the shearing-sheet framework that we have employed is inherently limited to address the conditions expected in the accretion disk boundary layer. For example, the absence of a hard-inner boundary could prevent Kelvin-Helmholtz instabilities from operating, see, e.g., Balsara et al. (2009). However, these instabilities do not seem to play a predominant role in the global MHD simulations of Armitage (2002) and Steinacker & Papaloizou (2002). Moreover, because we have assumed a constant background density, our analysis precludes the possibility of buoyant modes or convective instabilities. Whether these instabilities, and the turbulence they could drive, transport angular momentum inward or outward in Keplerian disks has been long debated (Ryu & Goodman 1992; Cabot 1996; Stone & Balbus 1996; Lesur & Ogilvie 2010). To our knowledge, these convective instabilities have not been studied in differentially rotating backgrounds with angular frequencies increasing outward; and speculating about their role goes beyond the scope of the present work.

In spite of the simplifications of our analytical study, the explicit solutions that we have found can provide physical insight and help elucidate transport processes in the inner disk regions close to a weakly magnetized accreting star. The current availability of powerful parallel codes (e.g. Stone et al. 2008) which are already being used to study the hydrodynamics of accretion disk boundary layers (Belyaev & Rafikov 2011) holds the promise that a more detailed understanding of MHD boundary layers will soon be possible.

MEP is grateful to the Knud Højgaard Foundation for its generous support. CKC is supported by a NORDITA fellow-

ship. We thank Tobias Heinemann, John Wettlaufer, and Jim Stone for useful discussions.

REFERENCES

Abramowicz, M., Brandenburg, A., & Lasota, J.-P. 1996, MNRAS, 281, L21
Armitage, P. J. 2002, MNRAS, 330, 895
—. 2010, Astrophysics of Planet Formation, ed. Armitage, P. J.
Balbus, S. A., & Hawley, J. F. 1991, ApJ, 376, 214
—. 1992a, ApJ, 400, 610
—. 1992b, ApJ, 392, 662
—. 1998, Reviews of Modern Physics, 70, 1
Balsara, D. S., Fisker, J. L., Godon, P., & Sion, E. M. 2009, ApJ, 702, 1536
Belyaev, M., & Rafikov, R. 2011, arXiv:1112.3102
Brandenburg, A., & Dintrans, B. 2006, A&A, 450, 437
Cabot, W. 1996, ApJ, 465, 874
Fan, Z., & Lou, Y.-Q. 1997, MNRAS, 291, 91
Frank, J., King, A., & Raine, D. J. 2002, Accretion Power in Astrophysics: Third Edition, ed. Frank, J., King, A., & Raine, D. J.
Goldreich, P., & Lynden-Bell, D. 1965, MNRAS, 130, 125
Goldreich, P., & Tremaine, S. 1978, ApJ, 222, 850
Goodman, J., & Xu, G. 1994, ApJ, 432, 213
Hartmann, L. 2009, Accretion Processes in Star Formation: Second Edition, ed. Hartmann, L. (Cambridge University Press)
Hawley, J. F., Gammie, C. F., & Balbus, S. A. 1995, ApJ, 440, 742
Heinemann, T., & Papaloizou, J. C. B. 2009, MNRAS, 397, 52
Hill, G. 1878, Am. J. Math, Vol. 1, No. 2, pp. 129-147
Inogamov, N. A., & Sunyaev, R. A. 2010, Astronomy Letters, 36, 848
Johnson, B. M. 2007, ApJ, 660, 1375
Kim, W.-T., & Ostriker, E. C. 2000, ApJ, 540, 372
Landau, L. D., & Lifshitz, E. M. 1959, Fluid mechanics, ed. Landau, L. D. & Lifshitz, E. M.
Lesur, G., & Ogilvie, G. I. 2010, MNRAS, 404, L64
Lithwick, Y. 2007, ApJ, 670, 789
Lynden-Bell, D., & Pringle, J. E. 1974, MNRAS, 168, 603
Medvedev, M. V. 2004, ApJ, 613, 506
Narayan, R., Goldreich, P., & Goodman, J. 1987, MNRAS, 228, 1
Narayan, R., & Popham, R. 1993, Nature, 362, 820
Pessah, M. E., Chan, C.-K., & Psaltis, D. 2006, MNRAS, 372, 183
—. 2008, MNRAS, 383, 683
Piro, A. L., & Bildsten, L. 2004, ApJ, 610, 977
Popham, R., Kenyon, S., Hartmann, L., & Narayan, R. 1996, ApJ, 473, 422
Popham, R., & Narayan, R. 1991, ApJ, 370, 604
—. 1995, ApJ, 442, 337
Popham, R., & Sunyaev, R. 2001, ApJ, 547, 355
Ryu, D., & Goodman, J. 1992, ApJ, 388, 438
Shakura, N. I., & Sunyaev, R. A. 1973, A&A, 24, 337
Snellman, J. E., Käpylä, P. J., Korpi, M. J., & Liljeström, A. J. 2009, A&A, 505, 955
Steinacker, A., & Papaloizou, J. C. B. 2002, ApJ, 571, 413
Stone, J. M., & Balbus, S. A. 1996, ApJ, 464, 364
Stone, J. M., Gardiner, T. A., Teuben, P., Hawley, J. F., & Simon, J. B. 2008, ApJS, 178, 137
Tagger, M., Pellat, R., & Coroniti, F. V. 1992, ApJ, 393, 708